INTERNATIONAL JOURNAL FOR NUMERICAL METHODS IN FLUIDS
Int. J. Numer. Meth. Fluids 2008; **57**:531–553
Published online 14 April 2008 in Wiley InterScience (www.interscience.wiley.com). DOI: 10.1002/fld.1803

Non-Newtonian flow in branched pipes and artery models

William L. Barth[1,*,†], Larisa V. Branets[2] and Graham F. Carey[3]

[1]*TACC, The University of Texas at Austin, Research Office Complex 1.405, J.J. Pickle Research Campus, Building 196, 10100 Burnet Road (R8700), Austin, TX 78758, U.S.A.*
[2]*ExxonMobil Upstream Research Company, 3319 Mercer St., NW509A, Houston, TX 77027-6019, U.S.A.*
[3]*CFDLab, ICES, The University of Texas at Austin, 1 University Station, Mail Code C0600, Austin, TX 78712, U.S.A.*

SUMMARY

This work concerns finite element analysis for a class of generalized Newtonian flows through branching pipe or tube junctions in industrial applications or blood flow through arterial branches, prosthetic tube implants or in biomedical engineering devices. A two-step morphing transformation is developed and implemented to map a generic coplanar 3D branching flow configuration to general out-of-plane deformed geometry including local constriction/dilation 'defects' suitable for modeling specific arterial flow and industrial flow applications. Unstructured 3D meshes may be generated in the reference configuration and morphed to the application configuration. The resulting meshes may be tangled and exhibit mesh quality degradation. Algorithms integrating mesh generation, morphing, untangling and cell shape control strategies are presented.

Phenomenological studies are conducted with the Powell–Eyring class as a representative model to determine local details of shear-thinning flow behavior as well as the nature and location of high shear stress regions on artery branch walls. The supporting simulations are carried out using a parallel finite element scheme with domain decomposition by a sectional partitioning that takes advantage of the medial curve shape and specialized ILU preconditioning. Copyright © 2008 John Wiley & Sons, Ltd.

Received 21 May 2007; Revised 17 February 2008; Accepted 19 February 2008

KEY WORDS: non-Newtonian flow; branching pipes and arteries; morphing transformations; mesh improvement; finite element methods; pressure boundary condition

*Correspondence to: William L. Barth, TACC, The University of Texas at Austin, Research Office Complex 1.405, J.J. Pickle Research Campus, Building 196, 10100 Burnet Road (R8700), Austin, TX 78758, U.S.A.
†E-mail: bbarth@tacc.utexas.edu

Contract/grant sponsor: Sandia National Laboratory
Contract/grant sponsor: Los Alamos National Laboratory

INTRODUCTION

There are numerous industrial applications that involve flow of Newtonian and non-Newtonian fluids through curved pipes, branching pipes and pipe networks where the flow behavior may be quite complex and high-resolution computations are warranted for reliable simulations. Analogous problems arise in biomedical applications such as modeling blood flow through branching arteries in the brain or cardiovascular system, and in prosthetic tube implants or other biofluidics or bioengineered support systems (see, e.g. [1–4]).

Biomedical applications involving living tissue are generally more complex because of patient-specific features, more complex biofluid rheology, the nature of tissue materials and uncertainty in properties and flow conditions. Here we focus on aspects concerning non-linear fluid models, geometry and mesh improvement, since the flow may be complex and the branching networks are more irregular, very out of plane and subject to strong local variations. Moreover, patient-specific modeling may be practically achieved by mapping from a generic model [5] and this may degrade numerical accuracy in the associated meshes unless mesh quality is controlled as seen later in this study.

Reliable simulations of certain engineering and biofluid problem classes may require fluid models of considerable complexity. For example, both industrial fluid suspensions and blood are frequently modeled qualitatively as Newtonian fluids, but other generalized viscosity models and more complex fluid models better characterize shear-thinning effects important in simulating near-wall behavior. For example, wall shear stress effects and effects of chemical blood thinners for stroke prevention are especially relevant in the context of the generalized viscosity models studied here. These viscosity models include, for instance, the Powell–Eyring, Williamson and Carreau fluids [6–8]. The Powell–Eyring model is taken as a representative example from this class in later numerical experiments. The flow problem is then discretized using an LBB-stable velocity–pressure finite element formulation for which optimal *a priori* estimates have been proven for the steady Powell–Eyring analog of Stokes flow [9]. The discretized non-linear problem is solved using a Newton scheme with Krylov subspace linear Jacobian system solves. The algorithm utilizes a domain decomposition approach for parallel simulation on distributed multiprocessor systems and is an extension of a scheme and software implementation for Navier–Stokes problems with Newtonian fluids [10–13]. An element-by-element approach is applied on independent subdomains. System preconditioning employs 'occasional' incomplete factorization of the Jacobian matrix, with the frequency of incomplete factorization determined automatically by the algorithm.

A further point of numerical interest in this work is the difficulty of generating meshes with well-shaped cells in regions where deformed branches intersect and the effect of such local mesh irregularity on the flow solution. In the accompanying numerical experiments and flow phenomenological studies, flow in coplanar branching pipes of constant cross section meeting at 120° is first considered as a generic 'base' configuration. This is used in baseline studies and then as the reference domain for morphing transformations to more general out-of-plane configurations. An unstructured, all-hexahedral mesh is generated using CUBIT [14] for the interior flow domain by extrusion of section meshes. Each arm of the flow domain is divided into four sections which divide the circular cross section into four quadrants. These sections are extruded from the flat, circular end along the length of the cylinder to the center of the domain where the three arms meet and are seamlessly joined. 'Baseline' flow solutions with different flow models are compared for this 'simple' reference domain. Following this, 'morphing' transformation functions are constructed to map the previous coplanar pipe geometry into more general shapes with out-of-plane deformed

DOI: 10.1002/fld

branches in 3D. This morphing approach is of general interest for branching pipe or tube flow geometries and is a novel approach for addressing problems related to meshing patient-specific data. This is illustrated here by flow simulations of shear-thinning fluids in some representative morphed geometries that are qualitatively based on part of a branched artery system in the human brain. As a result of this extreme morphing, the previous well-shaped mesh for pipes with coplanar medial axes is significantly deformed under the transformation, particularly in the branching subregion. A mesh improvement algorithm is introduced to untangle any overlapping cells and also improve general cell shape and size quality based on a recent quality metric formulation [15]. Variants of the associated algorithm are presented in this context. The flow is then computed on the resulting improved mesh. Both steady-state and pulsatile periodic flows are calculated and detailed flow studies conducted to investigate details of flow complexity and wall shear stress behavior due to shear-thinning effects near the branch region and local constrictions.

NON-NEWTONIAN FLOW MODEL

Incompressible laminar viscous flow of a generalized Newtonian fluid may be modeled by the momentum and continuity equations

$$\frac{\partial \mathbf{u}}{\partial t} + \mathbf{u} \cdot \nabla \mathbf{u} = \nabla \cdot \boldsymbol{\sigma}, \quad (\mathbf{x}, t) \in \Omega \times [0, t_f] \tag{1}$$

$$\nabla \cdot \mathbf{u} = 0 \tag{2}$$

where Ω is the spatial domain, t_f the final time of interest, $\mathbf{u}$ the unknown velocity vector, and $\boldsymbol{\sigma}$ the stress tensor.

The constitutive equation for the fluid stress has the form

$$\boldsymbol{\sigma} = -p\mathbf{I} + 2\mu \mathbf{D}(\mathbf{u}) \tag{3}$$

where $\mathbf{I}$ is the identity tensor, μ the (not necessarily constant) viscosity, and $\mathbf{D}(\mathbf{u})$ the strain rate tensor given by

$$\mathbf{D}(\mathbf{u}) = \tfrac{1}{2}(\nabla \mathbf{u} + (\nabla \mathbf{u})^{\mathrm{T}}) \tag{4}$$

Here, a class of generalized viscosity models that includes the Powell–Eyring, Williamson and Carreau models is considered. For certain choices of model parameters, these models reduce to the linear Newtonian model as a special case. A comparison of several viscosity models would be straightforward but is not the purpose of this work; hence, in the numerical simulations presented later, the Powell–Eyring model is taken as a representative case and compared only with the linear Newtonian fluid model.

The Powell–Eyring model is based on Eyring reaction rate theory which gives it a strong thermodynamic underpinning [6, 7, 16, 17]. This theory treats viscous diffusion as a 'rate process' described by a sum of exponential decay terms at the molecular level which leads to an expansion of the viscosity in terms of inverse hyperbolic sine functions. Retaining the first two terms in such an expansion leads to the 3-parameter Powell–Eyring model

$$\mu(s) = \mu_\infty + (\mu_0 - \mu_\infty) \frac{\sinh^{-1} \lambda s}{\lambda s} \tag{5}$$

DOI: 10.1002/fld

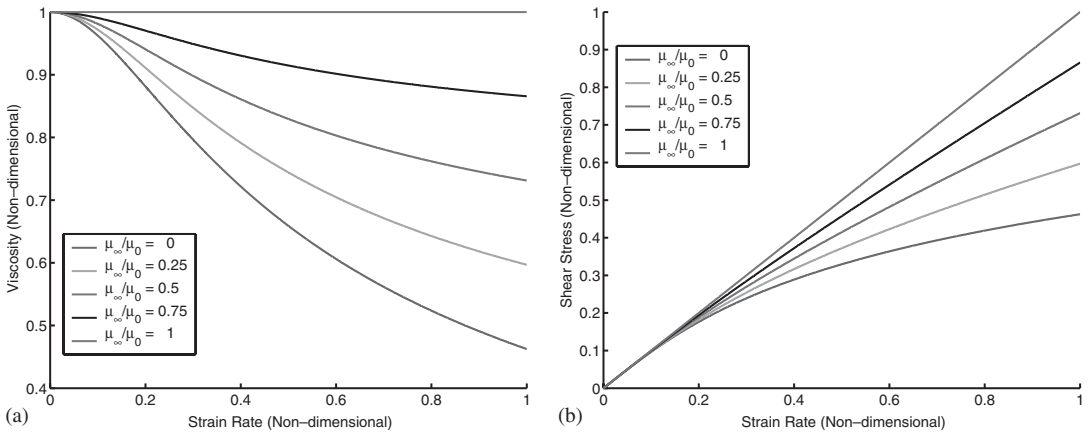

Figure 1. Powell–Eyring model: (a) viscosity and (b) shear stress.

where for strain rate s, μ_0 is the limiting viscosity at zero strain rate, μ_∞ the limiting viscosity as $s \to \infty$, and λ a characteristic time. The strain rate is given by

$$s(\mathbf{u}) = \sqrt{2\mathbf{D}(\mathbf{u}) : \mathbf{D}(\mathbf{u})} \tag{6}$$

Dimensionless viscosity $\mu(s)/\mu_0$ and shear stress magnitude, $s\mu(s)/s_0\mu_0$, are plotted in Figures 1(a) and (b) *versus* strain rate, s/s_0 for $\lambda = 100$ and five linearly spaced values of μ_∞/μ_0 in $[0, 1]$. Note that the familiar linear Newtonian case corresponds to $\mu(s)/\mu_0 = 1$. Comparison with the simpler Newtonian model is informative because it is often chosen for modeling viscous flow phenomena. Accuracy of this model becomes an issue here since shear-thinning and related wall shear effects are important. Such modeling error issues and their effect relative to discretization error have become a topic of increasing attention [18].

Remark

This shear-thinning fluid model has been suggested in the literature as a possible model for blood flow [19, 20]. Moreover, the monotone properties of the constitutive relation allow optimal finite element estimates to be proven and demonstrated for this fluid. This is generally true for the other fluids mentioned here, the exception being the extended Williamson fluid, primarily due to the behavior of the derivative of the stress at the origin shown by this fluid model [9, 13].

Initial and boundary conditions complete the specification of the mathematical problem. For time-dependent problems, an initial divergence-free velocity field is specified

$$\mathbf{u}(\mathbf{x}, 0) = g, \quad \mathbf{x} \in \Omega \tag{7}$$

On the solid walls of the domain Ω the usual no-slip and no-penetration conditions apply

$$\mathbf{u} = \mathbf{0}, \quad (\mathbf{x}, t) \in \Gamma_D \times [0, t_f] \tag{8}$$

where $\Gamma_D \subset \partial\Omega$.

DOI: 10.1002/fld

At the inflow and outflow boundaries ($\Gamma_p \subset \partial\Omega$) consider the following conditions:

$$(\boldsymbol{\sigma}(\mathbf{x},t)\cdot\hat{\mathbf{n}})\cdot\hat{\mathbf{n}} = \sigma_p(\mathbf{x},t) \tag{9}$$

$$\mathbf{u}\cdot\hat{\boldsymbol{\tau}}_1 = 0 \tag{10}$$

$$\mathbf{u}\cdot\hat{\boldsymbol{\tau}}_2 = 0, \quad (\mathbf{x},t)\in\Gamma_p\times[0,t_f] \tag{11}$$

where $\hat{\mathbf{n}}$ is the outward unit normal and $\hat{\boldsymbol{\tau}}_1$ and $\hat{\boldsymbol{\tau}}_2$ are unit tangent vectors to Γ_p. The first condition is a traction boundary condition and the latter two imply that there is no tangential flow at these boundaries; that is, flow is normal to inflow and outflow boundaries.

If surface Γ_p is perpendicular to the walls (as is the case in the branched geometries considered in subsequent flow simulations), then Equations (10) and (11) correspond to requiring that the flow be parallel to the walls at this boundary; otherwise they simply require the flow be normal to Γ_p. Equation (9) specifies the normal component of the surface traction force and is equivalent to a pressure boundary condition when used in conjunction with Equations (10) and (11) [13, 21]. Without these two tangential flow constraints, a pressure boundary condition on a flat surface is inconsistent with the underlying physics. Other outflow boundary conditions might also be considered for such cases where the desire for an imposed pressure drop can be relaxed [22–24].

WEAK FORMULATION AND FINITE ELEMENT IMPLEMENTATION

A weak variational formulation and corresponding Galerkin finite element scheme are used in subsequent numerical experiments. The associated weak formulation of the governing equations is derived in the same weighted residual manner as for Newtonian fluids by multiplying Equations (1) and (2) by appropriate velocity and pressure test functions, respectively, integrating over the domain Ω, and applying Gauss divergence theorem to the viscous stress term. By introducing the constitutive relations and setting velocity test functions to zero where essential conditions apply on the stationary solid walls, the weighted residual statement reduces to:

Find $(\mathbf{u}, p)\in\mathbf{V}\times Q$ satisfying the essential boundary conditions, (8), (10), and (11), and such that

$$\int_\Omega \rho\left(\frac{\partial\mathbf{u}}{\partial t}+\mathbf{u}\cdot\nabla\mathbf{u}\right)\cdot\mathbf{v}\,\mathrm{d}x = \int_\Omega p(\nabla\cdot\mathbf{v}) - 2\mu\mathbf{D}(\mathbf{u}):\nabla\mathbf{v}\,\mathrm{d}x + \int_{\Gamma_p}(\boldsymbol{\sigma}\cdot\hat{\mathbf{n}})\cdot\mathbf{v}\,\mathrm{d}s \tag{12}$$

$$-\int_\Omega q(\nabla\cdot\mathbf{u})\,\mathrm{d}x = 0 \tag{13}$$

for admissible test functions $(\mathbf{v}, q)\in\mathbf{V}\times Q$. Note that the normal traction has been retained in the boundary term arising from integration by parts.

The normal traction outflow boundary condition is applied by rewriting the boundary integral in Equation (12) as follows:

$$\int_{\Gamma_p}(\boldsymbol{\sigma}\cdot\hat{\mathbf{n}})\cdot\mathbf{v}\,\mathrm{d}s = \int_{\Gamma_p}(\boldsymbol{\sigma}\cdot\hat{\mathbf{n}})\cdot(v_{\hat{\mathbf{n}}}\hat{\mathbf{n}}+v_{\hat{\tau}_1}\hat{\boldsymbol{\tau}}_1+v_{\hat{\tau}_2}\hat{\boldsymbol{\tau}}_2)\,\mathrm{d}s \tag{14}$$

Substituting Equations (9) and (14) into Equation (12) and setting $v_{\tau_1}=v_{\tau_2}=0$, since the tangential velocity components are zero on Γ_p, the weak statement is: Find $(\mathbf{u}, p)\in\mathbf{V}\times Q$ satisfying the

DOI: 10.1002/fld

essential boundary conditions, (8), (10), and (11), and such that

$$\int_\Omega \rho\left(\frac{\partial \mathbf{u}}{\partial t}+\mathbf{u}\cdot\nabla\mathbf{u}\right)\cdot\mathbf{v}\,\mathrm{d}x=\int_\Omega p(\nabla\cdot\mathbf{v})-2\mu\mathbf{D}(\mathbf{u}):\nabla\mathbf{v}\,\mathrm{d}x+\int_{\Gamma_p}\sigma_p v_{\hat{\mathbf{n}}}\,\mathrm{d}s \tag{15}$$

$$-\int_\Omega q(\nabla\cdot\mathbf{u})\,\mathrm{d}x=0 \tag{16}$$

for all admissible test functions $(\mathbf{v},q)\in\mathbf{V}\times Q$.

Following [21] the condition of no flow tangential to Γ_p (Equations (10) and (11)) or, equivalently, that the flow to be entirely normal to inflow/outflow boundary sections, is enforced via a penalty approach as described next. The tangential velocity vector can be determined by subtracting the resolved velocity vector in the normal direction to obtain $[\mathbf{u}-(\mathbf{u}\cdot\hat{\mathbf{n}})\hat{\mathbf{n}}]$. The corresponding least-squares penalty functional on the boundary Γ_p then is

$$I(\mathbf{u})=\frac{1}{2\varepsilon}\int_{\Gamma_p}[\mathbf{u}-(\mathbf{u}\cdot\hat{\mathbf{n}})\hat{\mathbf{n}}]\cdot[\mathbf{u}-(\mathbf{u}\cdot\hat{\mathbf{n}})\hat{\mathbf{n}}]\,\mathrm{d}s \tag{17}$$

where $0<\varepsilon\ll 1$ is the penalty parameter. Taking the first variation, and simplifying, the contribution from the penalty functional is

$$\begin{aligned} I'(\mathbf{u})(\mathbf{v}) &= \frac{1}{\varepsilon}\int_{\Gamma_p}[\mathbf{u}-(\mathbf{u}\cdot\hat{\mathbf{n}})\hat{\mathbf{n}}]\cdot[\mathbf{v}-(\mathbf{v}\cdot\hat{\mathbf{n}})\hat{\mathbf{n}}]\,\mathrm{d}s \\ &= \frac{1}{\varepsilon}\int_{\Gamma_p}\mathbf{u}\cdot\mathbf{v}-(\mathbf{u}\cdot\hat{\mathbf{n}})(\mathbf{v}\cdot\hat{\mathbf{n}})\,\mathrm{d}s \end{aligned} \tag{18}$$

Adding this penalty contribution to the previous variational statement in Equation (15), the penalized problem implemented in subsequent numerical studies is:

Find $(\mathbf{u},p)\in\mathbf{V}\times Q$ satisfying the essential boundary conditions, (8), (10), and (11), and such that

$$\begin{aligned} \int_\Omega \rho\left(\frac{\partial \mathbf{u}}{\partial t}+\mathbf{u}\cdot\nabla\mathbf{u}\right)\cdot\mathbf{v}\,\mathrm{d}x &= \int_\Omega p(\nabla\cdot\mathbf{v})-2\mu D(\mathbf{u}):\nabla\mathbf{v}\,\mathrm{d}x \\ &\quad+\int_{\Gamma_p}\sigma_p v_{\hat{\mathbf{n}}}\,\mathrm{d}s+\frac{1}{\varepsilon}\int_{\Gamma_p}\mathbf{u}\cdot\mathbf{v}-(\mathbf{u}\cdot\hat{\mathbf{n}})(\mathbf{v}\cdot\hat{\mathbf{n}})\,\mathrm{d}s \end{aligned} \tag{19}$$

$$-\int_\Omega q(\nabla\cdot\mathbf{u})\,\mathrm{d}x=0 \tag{20}$$

for all admissible test functions $(\mathbf{v},q)\in\mathbf{V}\times Q$.

In the flow studies that follow, Equations (19) and (20) are discretized using the familiar continuous piecewise quadratic velocities and piecewise linear pressure bases for velocity and pressure, respectively. The resulting semidiscrete ordinary differential equation system is integrated in time using a second-order Adams–Bashforth/trapezoidal rule predictor–corrector method, and the resulting non-linear system in each time step is iteratively solved to a specified tolerance using Newton's method. The linear system at each Newton step is solved with SILU(0) preconditioned, element-by-element Bi-CGSTAB. The scheme is parallelized by partitioning elements into subdomains that are distributed to individual processors. Parallel scalability is enhanced through the

DOI: 10.1002/fld

use of non-blocking communication in the matrix–vector product routines employed in the linear solver. Further details of the numerical scheme can be found in [10–13, 21]. The methodology, flow simulation algorithms, and main viscous flow computer code have been verified against simple test problems with known analytic solutions and 'manufactured' solutions and against other numerical and experimental work in the literature [13].

NON-NEWTONIAN FLOW STUDIES

Branched pipe flows: We first compute time-dependent solution to steady state (where one exists) for pressure-driven flow in a branched pipe configuration. As there is no velocity scale in the problem statement, $\rho U^2 = \Delta\sigma$ is used in the traditional definition of the Reynolds number to arrive at a 'pressure' Reynolds number given by

$$Re = \frac{\rho U D}{\mu_0} = \frac{D\sqrt{\Delta\sigma\rho}}{\mu_0} \tag{21}$$

where D is the pipe diameter and $\Delta\sigma = |\sigma_{\text{in}} - \sigma_{\text{out}}|$ with σ_{in} and σ_{out} being the normal stress imposed at the inflow and outflow boundaries, respectively.

This choice of non-dimensionalization leads to a formulation of the problem that is consistent with the boundary conditions but where a change in the Reynolds number implies a change in the fluid as well (all other parameters being fixed). An alternate manner of non-dimensionalization of this problem is described in [21].

Figure 2 shows a diagram of the domain and boundary conditions used in the present simulation studies for the branched pipe problem. Each pipe section has non-dimensional diameter 1 and centerline length 5. The angle between the pipes is uniformly 120°. The outer surface of the pipe is a no-slip and no-penetration boundary. The single inflow section (on the right in the figure) has a fixed normal component of the traction, $(\hat{\boldsymbol{\sigma}} \cdot \hat{\mathbf{n}}) \cdot \hat{\mathbf{n}} = -1$, and the no-tangential flow condition is imposed. The two outflow sections of the boundary also have no-tangential flow with the normal component of the traction set to zero. The figure is colored with initial surface pressure contours. The initial velocity field is quiescent. The coplanar branched pipe geometry is meshed by dividing each arm into four quadrants, meshing one of the quadrants, and then duplicating this mesh through

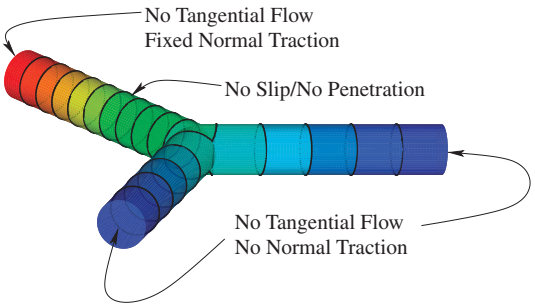

Figure 2. Branched pipe boundary condition diagram: color contours represent non-dimensional surface pressure between 0 (blue) and 1 (red).

DOI: 10.1002/fld

translation and rotation throughout the remainder of the quadrants and the other arms. In the present simulations this leads to a mesh of 23 040 elements using the CUBIT software [14] that has ∼600 000 degrees of freedom. This configuration is suitable for certain industrial applications and for medical equipment and prosthetic flow device simulation studies. Later, this configuration and mesh are morphed out of plane and the distorted mesh quality is improved by an optimization strategy prior to arterial flow simulation studies.

Coplanar geometry

In Figure 3, for $Re=10$, contours of velocity magnitude, the viscous stress magnitude, and pressure, are plotted for $\mu_\infty/\mu_0=1$, 0.1, and 0.01, on mid-pipe cross sections. There are 25 contour

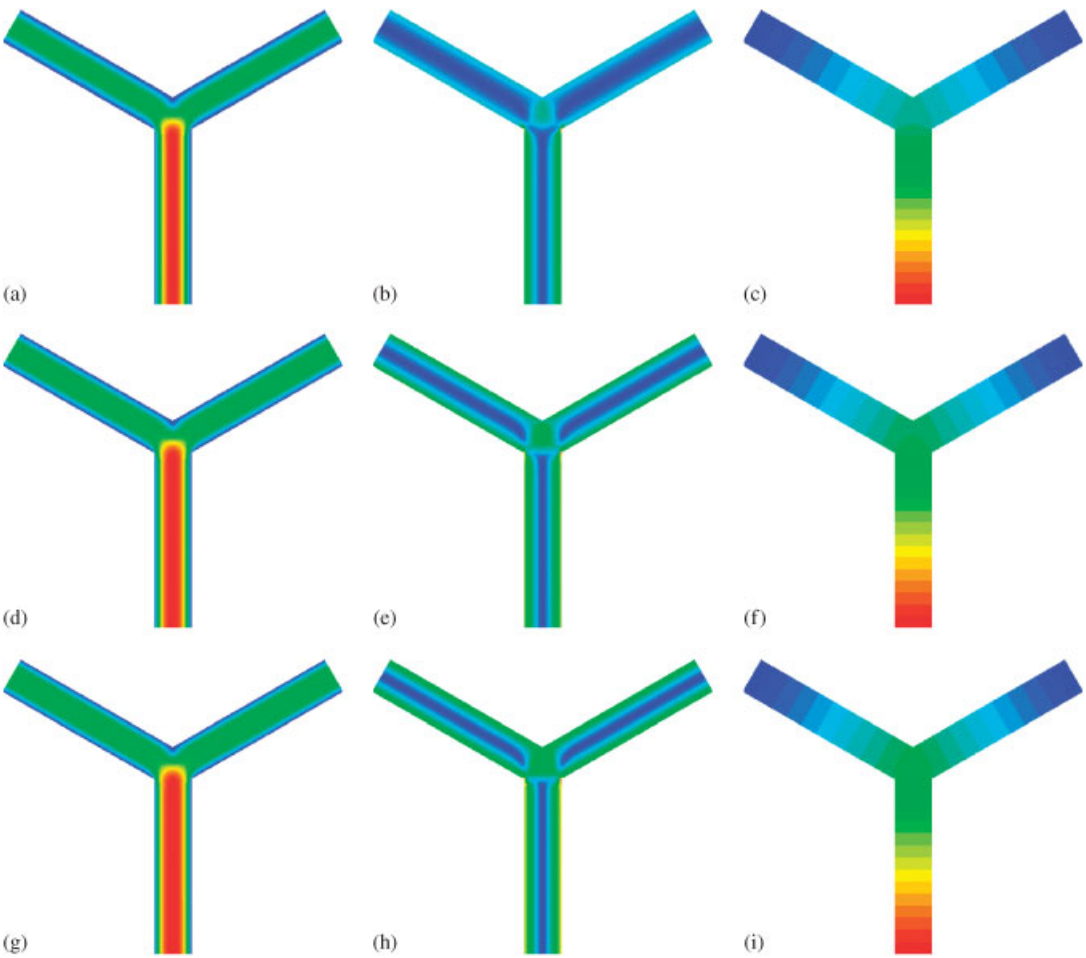

Figure 3. Effect of decreasing μ_∞/μ_0 at fixed Reynolds number, $Re=10$, Powell–Eyring fluid: (a) velocity magnitude, $\mu_\infty/\mu_0=1$; (b) viscous stress, $\mu_\infty/\mu_0=1$; (c) pressure, $\mu_\infty/\mu_0=1$; (d) velocity magnitude, $\mu_\infty/\mu_0=0.1$; (e) viscous stress, $\mu_\infty/\mu_0=0.1$; (f) pressure, $\mu_\infty/\mu_0=0.1$; (g) velocity magnitude, $\mu_\infty/\mu_0=0.01$; (h) viscous stress, $\mu_\infty/\mu_0=0.01$; and (i) pressure, $\mu_\infty/\mu_0=0.01$.

DOI: 10.1002/fld

levels on each plot, and the scale runs from the minimum (blue) to the maximum (red) of each quantity.

The contours of velocity magnitude clearly show that, as expected, the velocity profiles become more 'full' as μ_∞/μ_0 decreases. This change has little effect on the pressure distribution, only increasing it slightly adjacent to the stagnation point on the downstream wall at the branching joint. However, the local viscous stress magnitude shows a somewhat different behavior in the fully developed regions of the two 'arms' of the pipe network when compared with the Newtonian case. All cases show a linear variation from the maximum at the pipe wall to zero at the pipe centerline in the fully developed regions. In the Newtonian case, the stress at the pipe wall is considerably lower in the two arms than in the single inflow section. This reflects the fact that the flow rate and velocity magnitude in the outflow arms are half that of the inflow, and, therefore, the stress at the walls is similarly reduced. However, in the non-Newtonian cases, the stress has much larger magnitude in the fully developed region of the outflow arms in comparison with the inflow section, even though the velocity and flow rate are similarly halved. This effect becomes more pronounced as μ_∞/μ_0 is reduced and is due to the fuller profile shape in the downstream regions caused by the increasing effect of shear thinning.

In Figures 4–6, contours of velocity magnitude, viscous stress, and pressure, respectively, are plotted with $\mu_\infty/\mu_0=1$ in (a), 0.1 in (b), 0.025 in (c), and 0.01 in (d) at $Re=20$. These figures show the effect of increased convection in the problem. As μ_∞/μ_0 decreases, two recirculation regions have begun to appear just downstream of the junction on the upstream wall of each of the arms. This is due to the increasingly thin boundary layer, more plug-like flow in the interior,

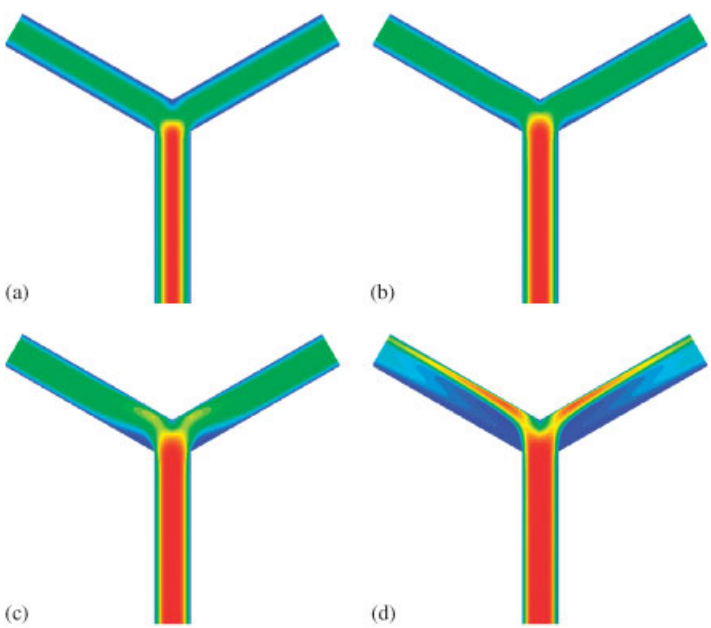

Figure 4. Contours of velocity magnitude, Powell–Eyring fluid with $Re=20$ for different viscosity ratios: (a) $\mu_\infty/\mu_0=1$; (b) $\mu_\infty/\mu_0=0.1$; (c) $\mu_\infty/\mu_0=0.025$; and (d) $\mu_\infty/\mu_0=0.01$.

DOI: 10.1002/fld

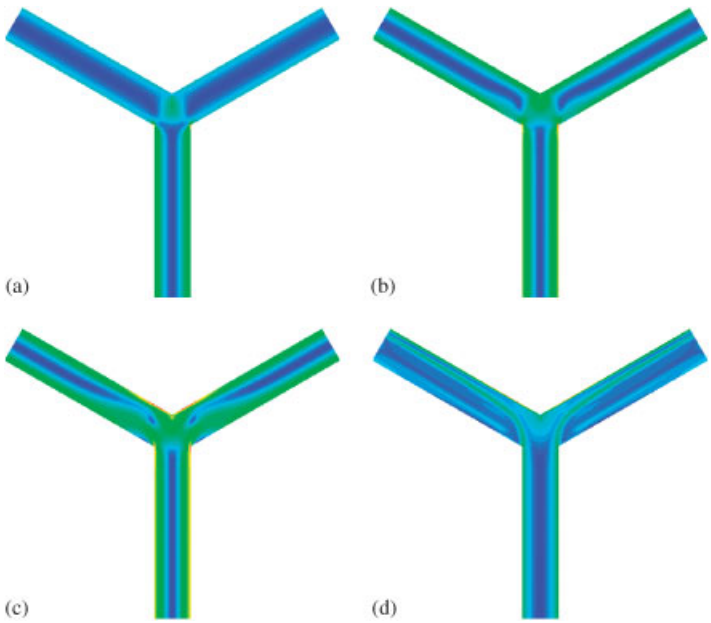

Figure 5. Contours of the magnitude of the viscous stress, Powell–Eyring fluid with $Re=20$ for different viscosity ratios: (a) $\mu_\infty/\mu_0=1$; (b) $\mu_\infty/\mu_0=0.1$; (c) $\mu_\infty/\mu_0=0.025$; and (d) $\mu_\infty/\mu_0=0.01$.

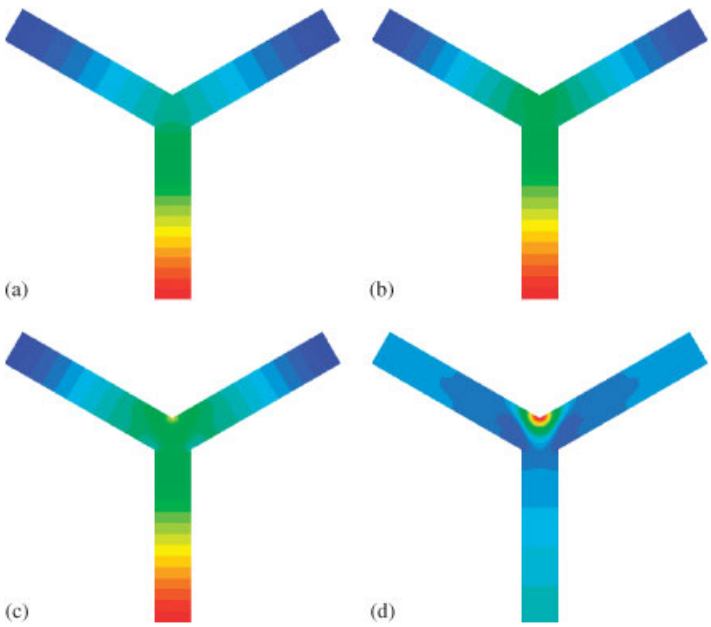

Figure 6. Pressure contours, Powell–Eyring fluid with $Re=20$ for different viscosity ratios: (a) $\mu_\infty/\mu_0=1$; (b) $\mu_\infty/\mu_0=0.1$; (c) $\mu_\infty/\mu_0=0.025$; and (d) $\mu_\infty/\mu_0=0.01$.

DOI: 10.1002/fld

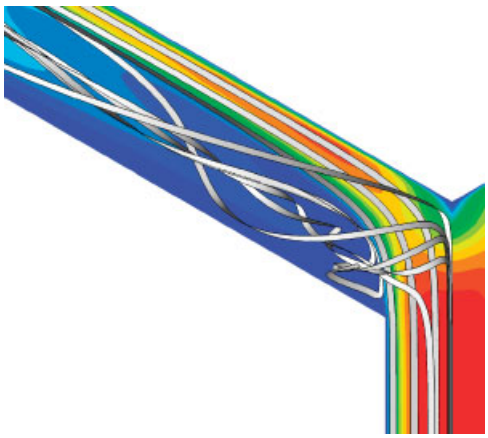

Figure 7. Stream ribbons illustrate twisting flow for $Re=20$ and $\mu_\infty/\mu_0=0.01$, Powell–Eyring fluid.

and higher maximum velocity. The adverse pressure gradient driving the recirculation flow can be seen in Figure 6(c). When $\mu_\infty/\mu_0=0.01$, the recirculation region is no longer a simple cell. The flow instead is strongly pushed away from the stagnation point where the pressure is even higher than at the inlet (see Figure 6(d)). Figure 7 shows, in detail, the local downstream effect of the increased stagnation pressure. In this figure, stream ribbons are plotted above a mid-plane of velocity magnitude contours. This close-up image shows that the flow above the mid-plane rises sharply near the stagnation point toward the top of the branch where it then cuts dramatically across toward the far wall. As it follows the curvature of the branch, flow turns down until it reaches the mid-plane and meets its symmetric counterpart from the bottom half of the branch. There a portion turns upstream, recirculates briefly, and turns back downstream near the branch centerline. The other part twists and turns downstream following the upstream wall of the branch. Now the flow is no longer completely laminar, and no fully developed region exists downstream of the bifurcation. This is a case where good, immersive, 3D visualization is required for a full understanding of the structures in the flow. 2D section plots and single images of streamlines do not effectively convey the nature of the flow.

Figure 5 shows locally high stresses in the neighborhood of the upstream junction of the branches as well as just downstream of the stagnation point. These higher stresses are present where the flow is turning most strongly, both at the first kink in the geometry encountered by the flow at the upstream junction, and as the flow near the centerline impinges on the downstream wall of each arm and is forced to turn parallel to it. It is also apparent in these figures that the complex flow that prevails here in the arms for $\mu_\infty/\mu_0=0.01$ leads to equally complex stress behavior. As there is no fully developed flow region in this case, the linear profile in the viscous stress no longer appears (see Figure 5(d)).

BRAIN ARTERY MODEL

The preceding discussion focused on branching pipe flows that may arise in traditional engineering applications involving Newtonian or non-Newtonian fluids. The non-Newtonian fluid model is

DOI: 10.1002/fld

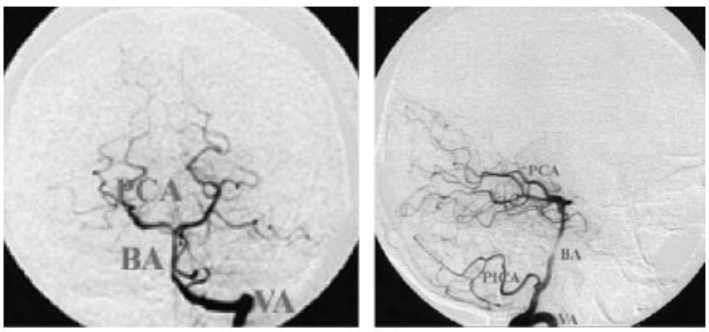

Figure 8. Two views of brain arteries (from http://www.neuropat.dote.hu/table/angio.htm).

a representative model that has been suggested as applicable for biofluids and the simulation methodology could be directly applied to analysis and design of biomedical engineering equipment for dialysis, heart assist, and other biomedical fluids uses. Our goal in the remainder of this paper is to conduct studies that extend this methodology toward the problem of simulating flows and drug delivery in arteries, more specifically in branching arteries. To facilitate this goal, morphing transformations are introduced to demonstrate the ideas for a geometric model of branching arteries in the brain. This is consistent with the notion of a map from a reference domain and the idea of eventually applying the same approach to morphing transformations for patient-specific data from medical imaging. This also allows us to capitalize on the mesh generation applied in the previous symmetric pipe studies and explore related mesh quality treatments to mitigate mesh errors associated with morphing. These issues are discussed in more detail in the following paragraphs. To motivate the model studies following, consider Figure 8 of patient brain artery scan data in the public domain (from http://www.neuropat.dote.hu/table/angio.htm). The figure displays branching artery configurations that may be a serious risk site for stroke. The left view shows the darker main branching structure of the arteries (BA-PCA) that supply a network of smaller arteries in the system. The right image shows that the upper branches are very out of plane. A larger inflow artery VA is also evident at the bottom of each view and a secondary branching artery (PICA) on the lower left of the right figure shows a branching geometry and again an out-of-plane character similar to that seen in BA-PCA. There is also geometric variation along the branches. These images of branching configurations were used as a guide in the geometric and flow modeling studies that follow. To that extent these studies are generic and designed to lead to a better understanding of qualitative effects due to out-of-plane deformation and branch constrictions. They are also preliminary insofar as patient-specific goals are concerned and we indicate how they may be extended to apply to individual data.

Morphing transformations

The previous symmetric uniform branched pipe configuration may be applied as a reference domain for geometric morphing to a desired tube or artery geometry model. In this reference branched pipe geometry, the symmetry axes of all three branches lie in the xz-plane, and the inflow branch symmetry axis follows the z-coordinate axis. Once an appropriate morphing transformation is constructed, it can be applied similarly to transform a mesh defined on the reference domain.

DOI: 10.1002/fld

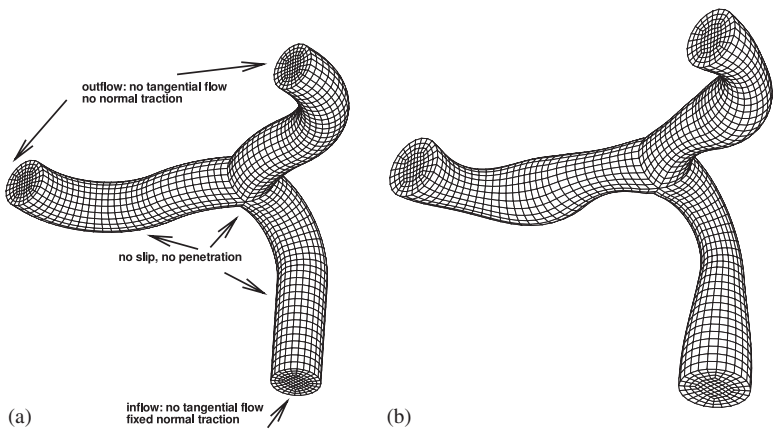

Figure 9. Domains and boundary conditions for the blood flow simulation: (a) without constrictions and (b) with constrictions.

This is the basic approach developed here for the out-of-plane artery branch model. The two representative examples of 3D out-of-plane meshed geometries shown in Figure 9 were obtained by applying a morphing transformation to the coplanar geometry and the associated hexahedral mesh used in the previous pipe flow studies. For each pipe branch, the deformation function is defined with the aim of modeling 3D branching arteries that may also have local constrictions or dilations. (The mapped domain and mesh on the left has uniform branches and that on the right has constrictions and dilations as discussed next.)

The morphing transformation leading to this curved 3D branch geometry is defined by two sets of deformation functions: The first transformation F_0 is used for morphing all three pipe branches from the reference configuration to create the underlying out-of-plane geometry (Figure 9(a)), and the second, F_c, is used for creating local constrictions and dilations (Figure 9(b)). The idea of using two transformations is representative of the general modeling workflow, where first transformation (e.g. F_0) is introduced to capture main geometric features and results in a generic (or 'healthy') model of the arteries. It is required only once, and the resulting geometry becomes a new 'reference' domain. The second transformation (e.g. F_c) is then designed to reproduce patient-specific variations from this generic model.

More specifically, in our case the out-of-plane deformation function for the inflow branch

$$F_0 = \begin{cases} x = x \\ y = R - (R - y)\cos(Rr) \\ z = r_0 + (R - y)\sin(Rr) \end{cases} \quad \text{if } r \leqslant \pi R/2$$

$$= \begin{cases} x = x \\ y = R + r - \pi R/2 \\ z = r_0 + R - y \end{cases} \quad \text{otherwise}$$

is chosen so that the symmetry axis of the branch ($r + r_0$, is the distance from the branch intersection point (origin) along this axis, where $r_0 = \text{const}$, $0 \leqslant r \leqslant r_{\max}$) would follow a quarter of a circle with

DOI: 10.1002/fld

radius $R=1.5\approx r_{\max}/\pi$, $r_{\max}=5$ in the yz-plane and then continue in a straight segment parallel to the y-axis. The constriction deformation function for the inflow branch

$$F_c=\begin{cases} x=\alpha x \\ y=\alpha y \\ z=z \end{cases} \quad \text{where } \alpha=1-0.1r\sin\left(\frac{3\pi r}{10}\right)$$

is designed for a flow to start from the widest part of the branch, then go through a constriction, which then widens into the branch intersection region. The superposition $F_c\circ F_0$ yields the morphing function for the inflow branch with constrictions as shown here. Similarly, the morphing function for each of the outflow branches is designed so that, starting from the branch intersection point, the axes of symmetry of the branches follow linked arcs of two circles in the (original) xz-plane and end in short straight segments parallel to the z-axis, as described by

$$\begin{aligned} F_0 &= \begin{cases} x=R+0.25-(3-1/2x-\sqrt{3}/2z)\cos\left(\dfrac{r+\pi}{3}\right) \\ y=y \\ z=\sqrt{3}(R+0.25)-1/\sqrt{3} \\ \quad -(3-1/2x-\sqrt{3}/2z)\sin\left(\dfrac{r+\pi}{3}\right) \end{cases} \qquad \text{if } r\leqslant\pi/2 \\ &= \begin{cases} x=R+0.25+(9/\pi-1+1/2x+\sqrt{3}/2z)\sin\left(\dfrac{r-\pi/2}{9/\pi-1}\right) \\ y=y \\ z=\sqrt{3}(R+0.25)-1/\sqrt{3}-2-9/\pi \\ \quad +(9/\pi-1+1/2x+\sqrt{3}/2z)\cos\left(\dfrac{r-\pi/2}{9/\pi-1}\right) \end{cases} \qquad \text{if } \pi/2\leqslant r\leqslant 4.5 \\ &= \begin{cases} x=R+0.25+9/\pi-1+1/2x+\sqrt{3}/2z \\ y=y \\ z=\sqrt{3}(R+0.25)-1/\sqrt{3}-2-9/\pi-r+4.5 \end{cases} \qquad \text{otherwise} \end{aligned} \tag{22}$$

The two outflow branches were morphed symmetrically with respect to the yz-plane and a higher-frequency constriction transformation with coefficient

$$\alpha=1+0.4\sin\left(\frac{7\pi r}{10}\right)$$

is used in order to introduce two constricted and two dilated sections in each branch.

Remark

Clearly, one can introduce other morphing functions from the planar reference domain to approximate a given target configuration defined by patient-specific data or by an 'average healthy branch

DOI: 10.1002/fld

configuration.' The latter may then become the new 'reference' domain and perturbation transformations away from this normal configuration introduced to study the effect of patient-specific pathology efficiently.

In the context of a particular patient-specific case, the mathematical framework for geometry morphing introduced in this section can be viewed in the following way. In general, deformation F_0 describes transformation of an object skeleton. In our example, the geometry of three branching straight segments (symmetry axes of pipes) should be mapped to a target patient-specific geometry skeleton. The target skeleton can be obtained from a medical image with the help of skeleton-based extraction methods (e.g. [25]) or deformable models (e.g. [26]) which yield approximation by splines. After skeletons are matched, deformation F_c defines transformation of the cylindrical pipe boundaries. Patient-specific boundary data are again obtained from an image, for example, using pattern-recognition [27] or an edge-detection algorithm which will result in piecewise polynomial or spline representation. Therefore, both mapping functions F_0 and F_c can be presented as piecewise analytical functions even for the patient-specific application. Moreover, radial symmetry of the boundary with respect to the medial axis is not a requirement of the general approach. Our use of the mesh improvement technique described in the following section eliminates the need for determining the volumetric transformation of the initial template geometry to a patient-specific case. Only the patient-specific boundary geometry is required as input.

Mapped mesh improvement

Viable non-folded meshes were generated in the original planar configuration as described earlier in this paper. The morphing transformations above are designed to map from the reference surface to the target surface. Similarly, they may provide a one-to-one correspondence between every point in the reference coplanar geometry and the new 3D branched geometry. Hence, when applied to every node in the reference mesh, they do not necessarily introduce element folding. However, there is obviously an effect on cell size and shape especially for cells near the branch intersection area and where mapping deformations are significant; hence, mesh quality will vary and will almost certainly deteriorate relative to the original mesh in the reference domain. (Here, a valid reference mesh of well-shaped cells is assumed.) To ameliorate cell quality degradation, mesh morphing may be followed by a corrective mesh optimization stage that is designed to improve the quality of cells that have been excessively deformed in shape under the map. This adds an additional step to the resulting algorithm.

The main steps in the composite algorithm then are as follows: (1) generate an unstructured 3D mesh in the reference domain; (2) define the transformations relating the target surface geometry to the reference surface geometry and morph the mesh to the target; (3) untangle and optimize the mesh to improve quality; (4) simulate the flow using the resulting mesh; and (5) use feedback and error indicators based on the computed solution to include error control in the optimization metric or adaptively refine the mesh locally.

Remark

For algorithm and application studies combining the mesh optimization approach with adaptive refinement see [28, 29].

Mesh improvement is generally applicable to the entire mesh but logically more important in the branching and local constriction/dilation areas. The main purpose here is to ensure that the overall mesh quality is good in a global optimization sense as described next. More specifically, the mesh smoothing framework in [15, 30, 31] is applied here and is based on controlling local cell

DOI: 10.1002/fld

shape distortion and dilation away from an ideal reference cell shape (a cube of average volume for hexahedral cells in the present work). To accomplish this, corresponding local distortion measures are introduced and combined to define a weighted composite local distortion and dilation metric $E_\theta(S)$ where S is the local Jacobian matrix of the map between the reference element $\hat{\Omega}_c$ and a physical cell in the morphed domain. The local mesh metric is defined in n-dimensions for a representative cell as a convex linear combination of a shape distortion metric $\beta(S)$ and a dilation metric $\mu(S)$

$$E_\theta(S) = (1-\theta)\beta(S) + \theta\mu(S), \quad 0 \leqslant \theta < 1 \tag{23}$$

with

$$\beta(S) = \frac{\left((1/n)\,\mathrm{tr}(S^{\mathrm{T}}S)\right)^{n/2}}{\det S}, \quad \mu(S) = \frac{1}{2}\left(\frac{1}{\det S} + \frac{\det S}{1}\right) \tag{24}$$

where parameter θ can be adjusted to emphasize distortion or dilation control and tr denotes the trace.

Integral contributions from the cells are accumulated to yield a global mesh distortion functional $\mathscr{I}$. This distortion functional achieves a minimum on an optimal (high-quality) mesh. That is, the mesh smoothing algorithm is formulated as a variational minimization problem

$$\min \mathscr{I} = \sum_c \int_{\hat{\Omega}_c} E_\theta(S)\,\mathrm{d}\boldsymbol{\xi} = \int_{\hat{\Omega}} E_\theta(S)\,\mathrm{d}\boldsymbol{\xi} \tag{25}$$

where $\hat{\Omega} = \cup_c \hat{\Omega}_c$. This minimization problem is solved here by applying an iterative descent optimization algorithm to a discretized form of functional (25).

The local shape and distortion cell metrics above achieve their minimum value 1 when $S = I$; that is, when reference and physical cells are identical. Similarly, the metrics approach infinity when a physical cell approaches degeneracy ($\det S \to 0$). The same behavior is preserved by the global distortion functional $\mathscr{I}$ and, under correct numerical approximation rules, by the discretized functional. Thus, an important property of this algorithm is that degenerate cells cannot be produced from valid cells during mesh smoothing (minimization of $\mathscr{I}$). Also, the functional can be modified to perform mesh untangling (i.e. mesh rectification starting from an invalid mesh with inverted elements) as well as smoothing.

The results of smoothing here are qualitatively similar to the improvement observed for hexahedral meshes under coplanar deformations where the lower branch angle is significantly reduced below 120° [15, 32]. For the present mesh with 9720 hexahedra, one iteration of the optimization smoothing procedure took about 15 s (on a PC with 2.2 GHz AMD processor), and about 100 s total time is required for mesh smoothing.

To test robustness under less favorable mapping conditions, the morphing transformations were next applied only to the boundaries of the original pipe mesh. Under this action, the interior mesh nodes are not mapped; hence, the mapped mesh is highly distorted with most elements that are adjacent to a boundary very elongated and many elements inverted. The untangling/smoothing algorithm developed in [30, 31] is then applied to generate a high-quality mesh inside the morphed boundaries. This extreme case required 30 iterations of the optimization algorithm and about 7 min total CPU time on the same PC. This algorithm produced essentially the same mesh as obtained previously from the more favorable fully mapped initial mesh. Hence, at moderate additional cost, this second approach allows more flexibility and expands the potential for modeling the geometry

DOI: 10.1002/fld

of real arteries from individual patient-specific data (where the boundary information is extracted from the image).

Remark

Note that this approach is also useful for dynamic simulations of fluid–structure interaction involving moving and naturally deforming walls or other flexible boundary surfaces or interfaces, as the morphing/smoothing/untangling procedure can also be performed fast in this case with smoothing requiring only 1 or 2 iterations.

Artery model flow simulations

The flow is computed with the improved meshes discussed above at $Re=10, 20$, and 50 (based, as remarked earlier for these apparent viscosity models, on the given pressure difference and μ_0) and with $\mu_\infty/\mu_0=1, 0.1, 0.03, 0.01$.

Figures 10–12 show the plots of viscous stress on the boundary and of interior flow streamlines, colored by pressure and velocity magnitude as appropriate, for the case $Re=20$ with branches without constrictions and at all stated choices of viscosity ratios. The color-scale range is defined by the maximum and minimum values over all four figures in order to facilitate comparison between the figures. The slow flow case, $Re=10$, does not exhibit significant changes with the change of μ_∞/μ_0, and at $Re=50$ vortices develop even for μ_∞/μ_0 close to 1, i.e. the Newtonian case. From these figures it is seen that

1. The largest boundary stresses occur at the non-smooth joints where the inflow branch meets the two other branches, and on the inside curve of the inflow branch. The area near the joint for the two outflow branches has very low stress in the case of a Newtonian fluid, but the wall stress in this region grows significantly with reduction of μ_∞/μ_0 (that is, for progressive shear thinning).
2. Pressure profiles are almost the same for all cases; however, pressure at the joint of the two outflow branches grows as μ_∞/μ_0 is reduced. That is, regions of higher pressure expand in the outflow direction.
3. The velocity of the fluid increases significantly with the non-linearity due to the apparent viscosity, and the velocity profile displays sharper gradients due to associated shear thinning. At $\mu_\infty/\mu_0=0.03$ a vortex starts to form near the joint for the outflow branches, and the vortex formation becomes more evident at $\mu_\infty/\mu_0=0.01$.

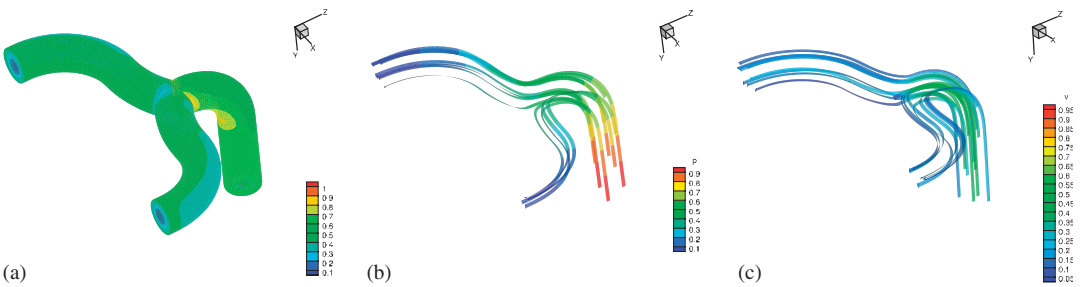

Figure 10. Flow at $Re=20$, $\mu_\infty/\mu_0=0.1$: (a) boundary stress; (b) pressure; and (c) velocity magnitude.

DOI: 10.1002/fld

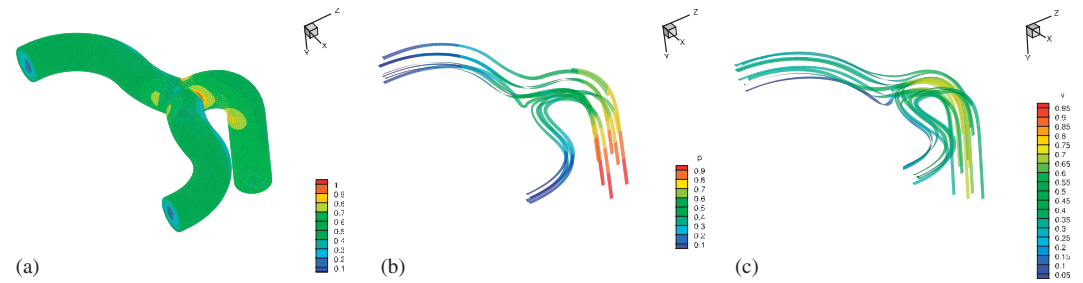

Figure 11. Flow at $Re=20$, $\mu_\infty/\mu_0=0.03$: (a) boundary stress; (b) pressure; and (c) velocity magnitude.

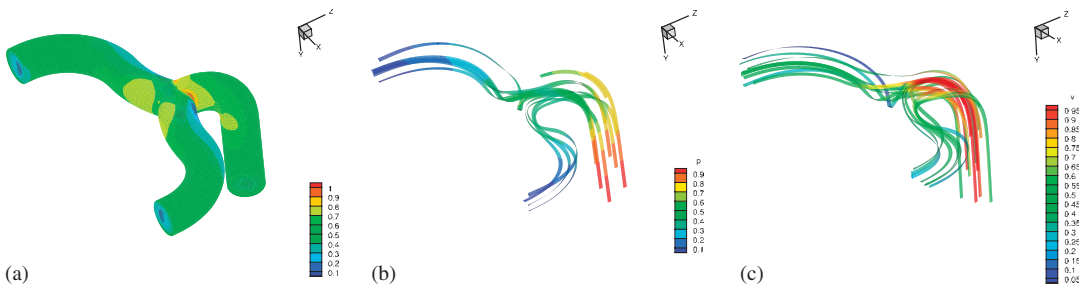

Figure 12. Flow at $Re=20$, $\mu_\infty/\mu_0=0.01$: (a) boundary stress; (b) pressure; and (c) velocity magnitude.

Figure 13 shows corresponding plots of boundary stress for various values of μ_∞/μ_0 and flow at $Re=20$ with local constrictions. The same trends in flow behavior with the change of μ_∞/μ_0 can be observed for this choice of geometry. However, the maximum boundary stress now occurs at the constriction in the inflow branch for the Newtonian flow, but is reduced for the non-Newtonian fluid, with implications concerning the effect of blood thinners on flow and wall shear near constrictions. Also the vortices do not form in this case. Figure 14 shows plots of stress, pressure, and velocity for the flow at $Re=20$, $\mu_\infty/\mu_0=0.01$. The color scales here are the same as in the previous figures. Comparing this result with that for flow under the same conditions in non-constricted branches (Figure 12), observe that constrictions reduce the non-linear effect of viscosity. That is, plots of velocity magnitude show a slower flow in the constricted injection branch with no vortices forming at the entry to the outflow branches. In addition, the boundary stress in this region is significantly lower for the constricted branch geometry.

Figure 15 shows a close-up view of the flow structure downstream of the bifurcation in the artery model with constrictions. The vortex structure is more apparent in this rendering and has a clearly different nature than that in the flat geometry as shown previously in Figure 7. In the artery model case, the upstream bend before the bifurcation causes the flow to accelerate as it rises. This acceleration causes the flow to pass by the bifurcation and follow the downstream wall down and away from the stagnation point creating a single vortex that fills the entire artery branch. In the flat geometry, the symmetry about the plane normal to the view direction allows the strong centerline flow upstream of the bifurcation to impinge on the downstream walls and split into symmetric upper and lower halves where two vortices fill the downstream part of the tube. Additionally, in the case of a drug delivery system and in the absence of diffusion, these ribbons

DOI: 10.1002/fld

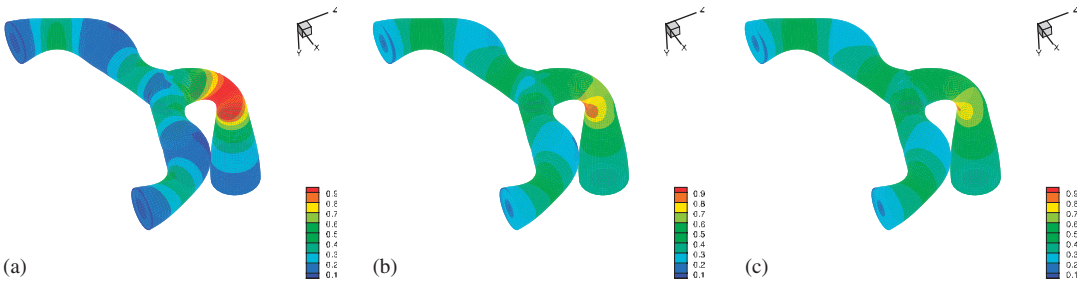

Figure 13. Boundary stress for flow in constricted branches at $Re=20$: (a) $\mu_\infty/\mu_0=1$; (b) $\mu_\infty/\mu_0=0.03$; and (c) $\mu_\infty/\mu_0=0.01$.

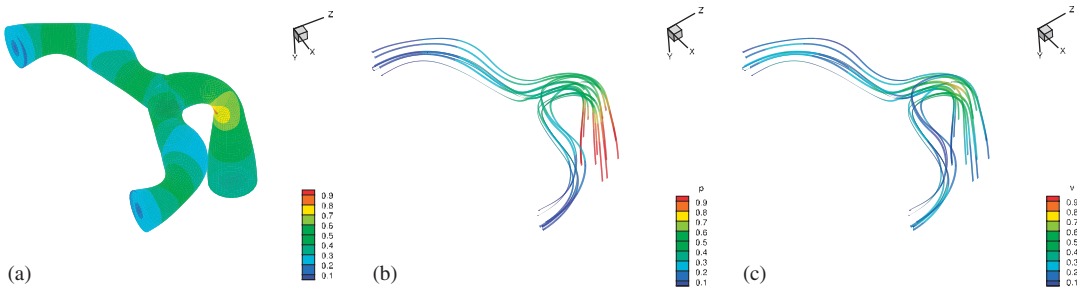

Figure 14. Flow in constricted branches at $Re=20$, $\mu_\infty/\mu_0=0.01$: (a) boundary stress; (b) pressure; and (c) velocity magnitude.

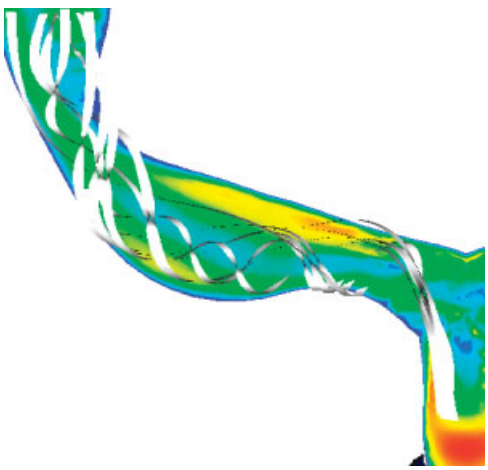

Figure 15. Stream ribbons illustrate flow in the brain artery model at $Re=20$ and $\mu_\infty/\mu_0=0.03$, Powell–Eyring fluid.

DOI: 10.1002/fld

give a 'first approximation advection model' of this additional transport process. The extension to include transient flow and diffusion effects is straightforward with our flow and transport simulation framework MGF [13] as the framework can accommodate up to 63 coupled transport PDEs in the system and provides a parallel HPC capability for easily adding further equations. Other effects such as chemical absorption on the walls, duration of delivery, and boundary conditions then become issues of interest. Such an extension is beyond the scope of this study and is the subject of continuing work.

Finally, in order to characterize the behavior of periodic blood flow in arteries better, transient 'pumping' flow simulations are performed. In these computations, instead of a fixed pressure gradient between inflow and outflow boundaries $\nabla p = -1$ (i.e. fixed normal traction on the inflow boundary), an oscillating pressure gradient $\nabla p = -0.5(1+\sin t)$ is specified. Simulations of periodic pumping flow at $Re = 20$ and $\mu_\infty/\mu_0 = 0.01$ yield similar results for both branch geometries (with and without constrictions). Representative plots of velocity magnitude at different times during periodic flow in the branched geometry without constrictions are shown in Figure 16. Since the flow has no time to fully develop under this specified transient pressure gradient and the periodic average pressure gradient is smaller than the value in the fixed gradient case, vortices do

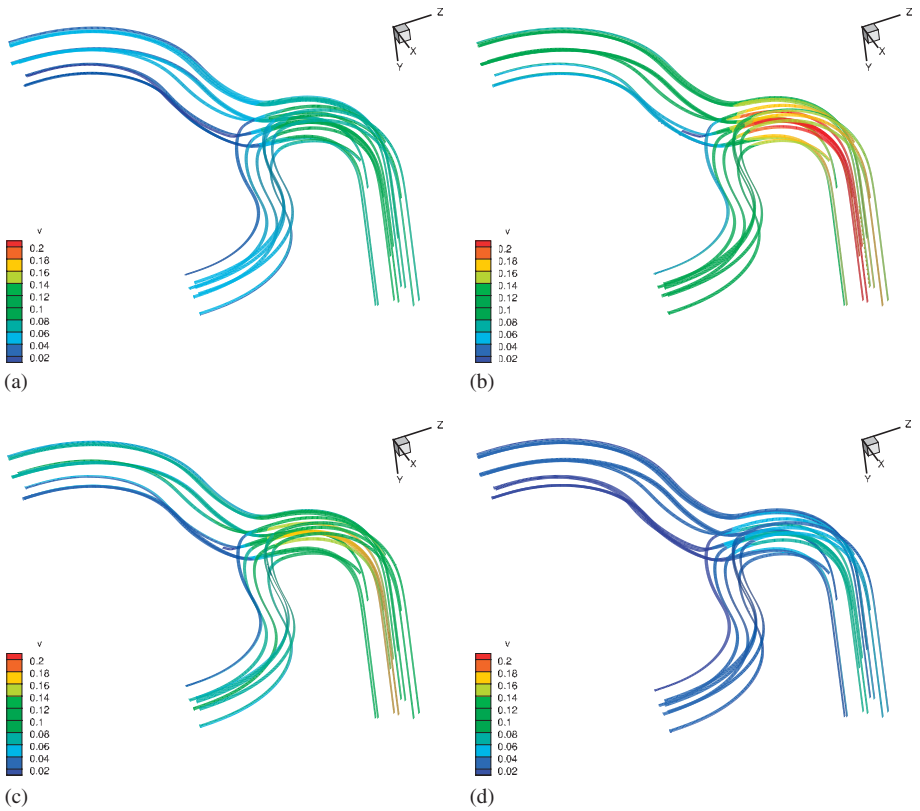

Figure 16. Pumping flow at $Re = 20$, $\mu_\infty/\mu_0 = 0.01$: velocity magnitude at different times: (a) $t = \pi/4$; (b) $t = 3\pi/4$; (c) $t = 5\pi/4$; and (d) $t = 7\pi/4$.

DOI: 10.1002/fld

not form in this example. (For example, compare with Figure 12, where vortices form at the same flow conditions but fixed pressure gradient.) Also, the maximum velocity magnitude, as well as the whole velocity profile, is similar to that of a Newtonian flow at $Re=20$ and fixed pressure gradient. Thus, in this test of a pumping flow the effects of the non-linear viscosity are not as significant.

CONCLUSIONS

In this study, our recent research work involving pressure-driven flow formulations, generalized viscosity models, and mesh improvement algorithms has been further developed and extended to study shear-thinning and wall stress effects in branching pipe and artery models. The resulting methodology is implemented and applied in a parallel non-linear viscous flow solver. The Powell–Eyring fluid model serves as a representative example of the generalized viscosity fluid class considered here. Numerical results for a range of viscosity parameters in the coplanar pipe studies illustrate that two recirculation zones begin to appear as the viscosity ratio is reduced and that the flow is simultaneously pushed away from the stagnation point in the branching zone. The flow behavior in this region is seen to be quite complex at these low ratios of viscosity parameters. More pronounced local stresses are also observed near the stagnation point in this case. In the parallel simulations, medial axis partitioning is shown to be very effective for this type of geometry with little communication overhead.

The geometry of more complex industrial branching configurations or artery branch models including local constrictions or dilations is approximated by introducing a morphing transformation that maps from a reference configuration into the design geometry. This morphing transformation can be applied simultaneously to the interior mesh or the mesh can be untangled as part of the subsequent mesh optimization strategy. Both work well here with the former slightly faster. However, the second test of the numerical scheme indicates the robustness of the mesh improvement algorithm and therefore the general suitability for maps that involve patient-specific data. This applies not only to this problem class but also to other applications. For example, in related work [15] this mesh quality metric is used to identify and improve ill-shaped cells in a patient-specific mesh for brain tumor surgical planning simulations [33]. The planar branching pipe configuration and mesh are the reference domain and mesh in this work, but the morphing transformation can be applied in the same manner twice—once as used here to an intermediate ‘normal’ artery branch model for qualitative baseline simulations and then to a ‘nearby’ model from patient-specific data for comparative simulations.

Numerical studies with the mapped artery model exhibit similar general features to those in the coplanar pipe study but some effects are more pronounced due to deformation of the geometry in the branching region in particular. Local constrictions and dilation in the branched geometry model also were studied with a view to the influence of such a local geometry variation on artery wall stress. In the case of a local constriction, the non-linear effects of the viscosity model are mitigated, the velocity is reduced and there is no vortex formation at the entry to the outflow branches for the case studied. Some exploratory simulations were made for the case of periodic ‘pumping’ flow with an oscillatory applied pressure gradient that has a lower mean value (0.5) than the previous case with fixed unit pressure gradient. This flow solution has a more benign behavior than the previous fixed case as one would anticipate. More numerical and parametric studies are needed to explore the range of behaviors in the branching subregion for this periodic transient case.

DOI: 10.1002/fld

The geometry map and mesh improvement strategy also appear suitable for extension to future applications involving moving and deforming boundaries: For example, in an explicit geometry update strategy, the geometry change computed from the prior fluid–structure analysis time step can be used to provide the data for updating the morphing map; the mesh improvement algorithm then does a very fast 'remap' of the mesh ensuring good cell quality. The solution field is projected to the new mesh and the solution step continues. Such schemes can be utilized efficiently for specified large deformations of the branches (due to breathing or impact to torso and head arteries) or to smaller changes in an artery boundary due to pulsatile flow.

The methodology, morphing, and mesh improvement algorithms are essentially independent of the application cell choice; hence, one could equally apply this to other engineering and biomedical applications using, for instance, tetrahedral cells instead of hexahedra. An interesting feature of the present approach is that the 3D mesh in a reference domain can be generated once and archived to be morphed into different specific applications and optimized as described here. Other configurations can be similarly archived and linked to form a larger more complex network. For instance, one could connect numerous curved and branching 'component segments' to integrate them into a more global network model of a complex system. The morphing and mesh generation strategies would be applied at the local component level ensuring compatibility across the 'interfaces' between components. Of course, such a multicomponent linked system would be correspondingly more computationally intensive and the parallel algorithm and specialized preconditioner applied here would be essential to timely predictive simulation. In this respect, the present methodology and software are starting points for more specific studies and broader studies that could be made with medical researchers conducting experiments or evaluating treatments. The brain arteries would appear to provide a greater challenge to such experimental studies but the qualitative results shown here and the ability to study the effects of blood thinners may be more tractable. Studies of prosthetic device performance would also be more amenable to comparison.

ACKNOWLEDGEMENTS

Research and development work for this study was carried out in the CFDLab at the University of Texas at Austin and large-scale computations were carried out on the parallel cluster system at the Texas Advanced Computing Center (TACC). The support for some of the mesh research and software development was provided by grants from Sandia and Los Alamos National Laboratories.

REFERENCES

1. Haselton FR, Scherer PW. Flow visualization of steady streaming in oscillatory flow trough a bifurcating tube. *Journal of Fluid Mechanics* 1982; **123**:315–333.
2. Liepsch D, Poll A, Mijovic B, Pflugbeil G. Flow studies in rigid and elastic y-junction models using Newtonian and non-Newtonian fluid. *Advances in Bioengineering* (ASME) 1992; **22**:277–280.
3. Gijsen FJH, van de Vosse FN, Janssen JD. The influence of the non-Newtonian properties of blood on the flow in large arteries: steady flow in a carotid bifurcation model. *Journal of Biomedics* 1999; **32**:601–608.
4. Mijovic B, Liepsch D. Experimental flow studies in an elastic y-model. *Technology and Health Care Archive* 2003; **11**:115–141.
5. Miller K, Joldes GR, Lance D, Wittek A. A total Lagrangian explicit finite dynamics algorithm for computing soft tissue deformation. *Communications in Numerical Methods in Engineering* 2007; **23**:121–134.
6. Ree T, Eyring H. Theory of non-Newtonian flow. II. Solution system of high polymers. *Journal of Applied Physics* 1955; **26**:800–809.
7. Eyring H. Viscosity, plasticity, and diffusion as examples of absolute reaction rates. *Journal of Chemical Physics* 1936; **4**:283–291.

DOI: 10.1002/fld

8. Cramer SD, Marchello JM. Numerical evaluation of models describing non-Newtonian behavior. *AIChE Journal* 1968; **14**:980–983.
9. Chow S, Carey G. Finite element approximations of generalized Newtonian fluids. *Technical Report*, TICAM, The University of Texas at Austin, 2001.
10. Carey GF, McLay R, Barth W, Swift S, Kirk B. Distributed parallel simulation of surface tension driven viscous flow and transport processes. *Computational Fluid Dynamics*: *Proceedings of the Fourth UNAM Supercomputing Conference*, Mexico City, Mexico, UNAM, June 2000; 143–155.
11. Barth W, Carey GF, Kirk B, McLay R. Parallel distributed solution of viscous flow with heat transfer on workstation clusters. *High Performance Computing '00 Proceedings*, Washington, DC, April 2000.
12. Barth W, Carey GF, Chow S, Kirk B. Finite element modeling of generalised Newtonian flows. *Proceedings of the 14th Australasian Fluids Conference*, Adelaide, December 2001.
13. Barth WL. Simulation of non-Newtonian fluids on workstation clusters. *Ph.D. Thesis*, The University of Texas at Austin, May 2004.
14. *Cubit Mesh Generation Toolkit*. 2008. Available from: http://cubit.sandia.gov/.
15. Branets LV. A variational grid optimization method based on a local cell quality metric. *Ph.D. Thesis*, The University of Texas at Austin, August 2005.
16. Ree T, Eyring H. Theory of non-Newtonian flow. I. Solid plastic system. *Journal of Applied Physics* 1955; **26**:793–800.
17. Ree FH, Ree T, Eyring H. Relaxation theory of transport problems in condensed systems. *Industrial Engineering and Chemistry* 1958; **50**:1036–1040.
18. Carey GF, Barth W, Woods J, Kirk B, Anderson M, Chow S, Bangerth W. Modeling error and constitutive relations in simulation of flow and transport. *International Journal for Numerical Methods in Fluids* 2004; **46**:1211–1236.
19. Russell CP, Christiansen EB. Axial, laminar, and non-Newtonian flow in annuli. *Industrial and Engineering Chemistry*, *Process Design and Development* 1974; **13**(4):391–396.
20. Christiansen EB, Craig JSE, Carter TR. The effect of temperature on the consistency of fluids. *Transactions of the Society of Rheology* 1966; **10**(1):419–430.
21. Barth WL, Carey GF. On a boundary condition for pressure-driven laminar flow of incompressible fluids. *International Journal for Numerical Methods in Fluids* 2007; **54**:1313–1325.
22. Griffiths DF. The 'no boundary condition' outflow boundary condition. *International Journal for Numerical Methods in Fluids* 1997; **24**:393–411.
23. Bose A, Carey GF. Least-squares *p–r* finite element methods for incompressible non-Newtonian flows. *Computer Methods in Applied Mechanics and Engineering* 2000; **180**:431–458.
24. Yagawa G, Eguchi Y. Comparison between the traction and pressure-imposed boundary conditions in finite element flow analysis. *International Journal for Numerical Methods in Fluids* 1986; **7**(5):521–532.
25. Prinet V, Ge OMC, Xie S, Ma S. Thin network extraction in 3d images: application to medical angiograms. *Proceedings of the International Conference on Pattern Recognition*, Vienna, Austria, 1996; 386–390.
26. Klein A, Lee F, Amini A. Quantitative coronary angiography with deformable spline models. *IEEE Transactions on Medical Imaging* 1997; **16**:468–482.
27. Kawata Y, Niki N, Kumazaki T, Moonier P. Characteristics measurement for blood vessel diseases detection based on cone-beam CT images. *IEEE Nuclear Science Symposium and Medical Imaging Conference*, San Francisco, CA, vol. 3, 1995; 1660–1664.
28. *libMesh*: *A* c++ *Finite Element Library*. 2008. Available from: http://libmesh.sourceforge.net/.
29. Carey GF. *Computational Grids*: *Generation*, *Adaptation*, *and Solution Strategies*. Taylor and Francis: London, 1997.
30. Branets L, Carey GF. A local cell quality metric and variational grid smoothing algorithm. *Proceedings of the 12th International Meshing Roundtable*, Santa Fe, NM, 2003; 371–378.
31. Branets L, Carey GF. A local cell quality metric and variational grid smoothing algorithm. *Engineering with Computers* 2005; **21**:19–28.
32. Branets L, Carey GF. Smoothing and adaptive redistribution for grids with irregular valence and hanging nodes. *Proceedings of the 13th International Meshing Roundtable*, Williamsburg, VA, 2004; 333–344.
33. Miller K. *Biomechanics of Brain for Computer Integrated Surgery*. Warsaw University of Technology Publishing House: Warsaw, 2002.

DOI: 10.1002/fld